Quantized spin-wave modes in magnetic tunnel junction nanopillars

A. Helmer,[1,2,*] S. Cornelissen,[3,4] T. Devolder,[1,2] J.-V. Kim,[1,2] W. van Roy,[3] L. Lagae,[3,5] and C. Chappert[1,2]

[1]*Institut d'Electronique Fondamentale, UMR CNRS 8622, 91405 Orsay, France*
[2]*Université Paris-Sud, 91405 Orsay, France*
[3]*IMEC, Kapeldreef 75, 3001 Leuven, Belgium*
[4]*ESAT, KU Leuven, Leuven, Belgium*
[5]*Natuurkunde en Sterrenkunde, KU Leuven, Leuven, Belgium*

We present an experimental and theoretical study of the magnetic field dependence of the mode frequency of thermally excited spin waves in rectangular-shaped nanopillars of lateral sizes 60×100, 75×150, and 105×190 nm^2, patterned from MgO-based magnetic tunnel junctions. The spin-wave frequencies were measured using spectrally resolved electrical-noise measurements. In all spectra, several independent quantized spin-wave modes have been observed and could be identified as eigenexcitations of the free layer and of the synthetic antiferromagnet of the junction. Using a theoretical approach based on the diagonalization of the dynamical matrix of a system of three coupled, spatially confined magnetic layers, we have modeled the spectra for the smallest pillar and have extracted its material parameters. The magnetization and exchange stiffness constant of the CoFeB free layer are thereby found to be substantially reduced compared to the corresponding thin-film values. Moreover, we could infer that the pinning of the magnetization at the lateral boundaries must be weak. Finally, the interlayer dipolar coupling between the free layer and the synthetic antiferromagnet causes mode anticrossings with gap openings up to 2 GHz. At low fields and in the larger pillars, there is clear evidence for strong nonuniformities of the layer magnetizations. In particular, at zero field, the lowest mode is not the fundamental mode but a mode most likely localized near the layer edges.

I. INTRODUCTION

In the last few years, magnetic tunnel junction (MTJ) nanopillars have received tremendous attention due to their promising potential for applications in spin-transfer-switched magnetoresistive random access memory or as spin-torque oscillators for microwave generation.[1–3] With gigahertz frequencies, the operation speed of these devices happens to lie in the same frequency range as the dynamic eigenexcitations of the underlying nanoelements (thermally excited spin waves), which may therefore manifest themselves as unwanted noise sources. However, as eigenexcitations, thermal spin waves also constitute an excellent probe for the intrinsic magnetic properties of the nanopillars. The experimental detection of spin waves in MTJ nanopillar devices and the understanding of their nature is therefore of great interest both for fundamental and technological reasons.

Thermal spin waves in confined structures have been studied extensively in arrays of single-layer dots with thicknesses between 40 and 15 nm and typical lateral dimensions from 3 μm down to 200 nm.[4–8] In these systems, two types of spin-wave modes have been identified: quantized volume modes located around the center of the element where the internal field is basically homogeneous, and spin-wave well, end or edge, modes localized near the element edges in the inhomogeneity region of the internal field. The above elements are characterized by their thickness being significantly larger than the exchange length of the layer material (typically 5 nm). In structures with this property, the dominating interaction is the magnetostatic dipolar interaction,[9] which causes the inhomogeneity of the internal field, thus determining the character and spatial profile of the modes.[4]

The eigenexcitations of a multilayer dot differ, in general, significantly from those of an ensemble of isolated magnetic dots due to the interlayer interactions between the magnetic layers in the stack: mutual dipolar coupling and—for sufficiently thin metallic spacer layers—interlayer exchange coupling.[10]

Eigenexcitations of nanopillar structures have been the subject of very few systematic studies so far. Thermal spin waves have been investigated experimentally and theoretically in pseudospin valves[11–13] of elliptical shape (smallest dimension 200 nm) consisting of two magnetic layers of 10 nm thickness separated by a 10-nm-thick spacer layer. As the layer thicknesses were (again) much larger than the exchange length, the profiles of the modes in each of the two pillar layers showed great resemblance with the mode profiles in the corresponding isolated dots.[7] In a symmetric spin-valve stack, the main impact of the mutual dipolar coupling between the layers was found to be a fixed phase relation between the modes in the two layers for high applied field and hybridization effects at low field.[11]

Common MTJ nanopillars differ qualitatively from the pseudospin valves in three fundamental points: First, with a free layer (FL) and a synthetic antiferromagnet (SAF), they consist of three magnetic layers. Second, the layer thicknesses are with 2–4 nm smaller than the exchange length, such that the spin dynamics is now dominated by the exchange interaction. Third, the interlayer interaction of the three layers is highly asymmetric: the reference layer (RL) and the pinned layer (PL) of the SAF are strongly coupled by the interlayer exchange and—more weakly—the mutual dipolar coupling, where the PL is additionally subject to the strong exchange-bias field; the FL interacts with the SAF via the comparatively weak mutual dipolar coupling only. Con-

sequently, the eigenexcitations of an MTJ nanopillar are expected to be considerably more complex than those of the pseudospin valves.

Magnetization dynamics in MTJ nanopillars is commonly measured using electrical techniques, such as electrical-noise power measurements[13–16] or spin-transfer-driven ferromagnetic resonance,[17] which take advantage of the correspondence of the magnetoresistance (MR) of the pillar and the spin dynamics in the FL and the RL. Thermal spin-wave modes in MTJ have been detected as "by-products" of experiments on spin-transfer torque[3,14,18] and in a few dedicated experiments.[16] However, so far there has been no systematic study of thermal excitations in MTJ nanopillars.

In this paper, we investigate the magnetic field dependence of the mode frequency of thermally excited spin waves in rectangular-shaped MgO-based MTJ nanopillars of different lateral sizes. In Sec. II, we will describe the basic magnetic properties of the devices and the experimental technique used to acquire the spin-wave spectra. The features of the measured spectra in dependence of the pillar size and the direction of the applied field are described in the following Sec. III. In Sec. IV, we will point out shortcomes of the macrospin model when applied to our samples, as a consequence of which we will introduce in Sec. V a model of quantized spin-wave modes in nanopillars consisting of three magnetic layers. In Sec. VI, we will use this model to extract the material parameters of the pillar, which will finally be discussed in Sec. VII along with the limitations of our model.

II. SAMPLES AND EXPERIMENTAL TECHNIQUES

A. Samples and basic device properties

The fabrication and basic properties of our samples are described in Ref. 19: they are rectangular-shaped nanopillars, all patterned from the same MTJ stack of composition $Co_{60}Fe_{20}B_{20}$ (3 nm, free layer)/Mg(1.3) [nat. ox.]/$Co_{60}Fe_{20}B_{20}$ (2, reference layer)/Ru(0.8)/$Co_{70}Fe_{30}$ (2, pinned layer)/PtMn(20), deposited by Singulus Technologies AG. The three layers following the MgO tunnel barrier compose the SAF. The pillars were designed in three lateral sizes: 60×100, 75×150, and 105×190 nm², which will be referred to as small (S), medium (M), and large (L) size, respectively. Note that unlike in Ref. 19, the given dimensions are not the nominal values but mean values measured on the exposed e beam resist with a device-to-device deviation of ± 10 nm. In order to obtain electrically contactable devices, the nanopillars were inserted in series between coplanar leads, following design rules ensuring high bandwidth.[20]

The devices have a resistance area product of 16 Ω μm^2 and typically 80% tunnel magnetoresistance ratio. Their hysteretic properties are consistent with the uniaxial anisotropy expected from the rectangular pillar shape where the long edge of the rectangle, oriented along the exchange pinning direction of the PtMn antiferromagnet, is the easy axis (EA), and the short edge the hard axis (HA) of the magnetization. Panels (b) and (d) of Fig. 1 show as a reference EA and HA
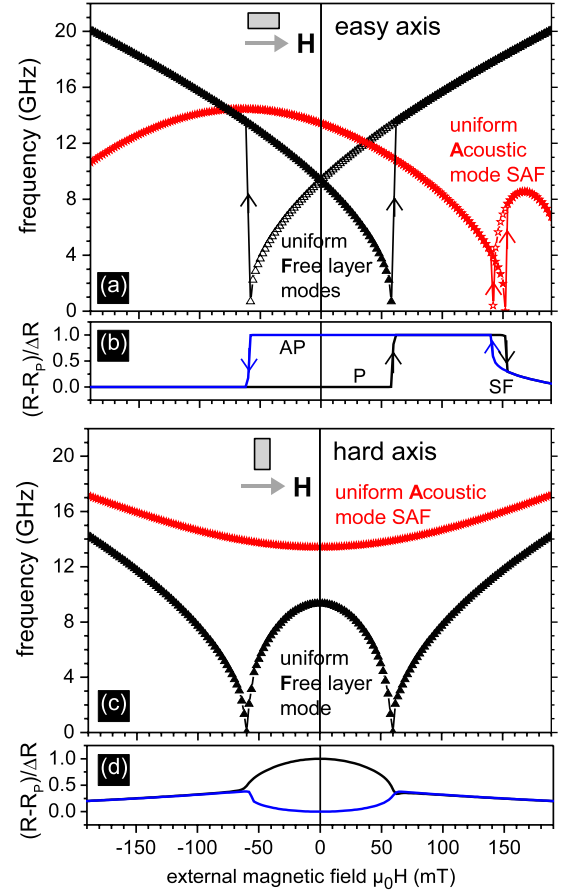

FIG. 1. (Color online) Macrospin description of a nanopillar of size S: frequencies of the uniform modes versus external field along (a) easy axis and (c) hard axis, calculated in macrospin approximation using as material parameters literature bulk or thin-film values (see Appendix B2): magnetization 2.2 T for CoFe, 1.9 T for annealed CoFeB, exchange bias $J^{eb}=4.5\times10^{-4}$ J/m², interlayer exchange $J^{int}=-5\times10^{-4}$ J/m²; the shape anisotropy fields were calculated using demagnetizing factors extracted from OOMMF simulations. Panels (b) and (d) show the corresponding calculated hysteresis loops. In panel (a), filled symbols are used for ascending field (P→AP→SF) and open symbols for descending field (SF→AP→P).

hysteresis loops of a nanopillar of size S calculated in macrospin approximation using as material parameters literature bulk values (see figure caption). In comparison, the experimental EA and HA loops for devices of pillar size S, M, and L are depicted in panels (b), (d), and (f) of Figs. 2 and 3, respectively.

At negative EA applied fields, the pillars are in the parallel (P) state, at positive fields in the antiparallel (AP) state; spin-flop (SF) transition of the SAF occurs typically at EA fields around +170 mT. Room-temperature coercivity is 25–35 mT for devices of size S and M, and 20–25 mT for size L. From astroid measurements[19] mean anisotropy fields of 37 mT, 46 mT, and 38 mT for pillar sizes S, M, and L, respectively, have been determined. The EA loops of all devices are off-centered toward negative fields, indicating non-negligible antiparallel coupling of the free-layer
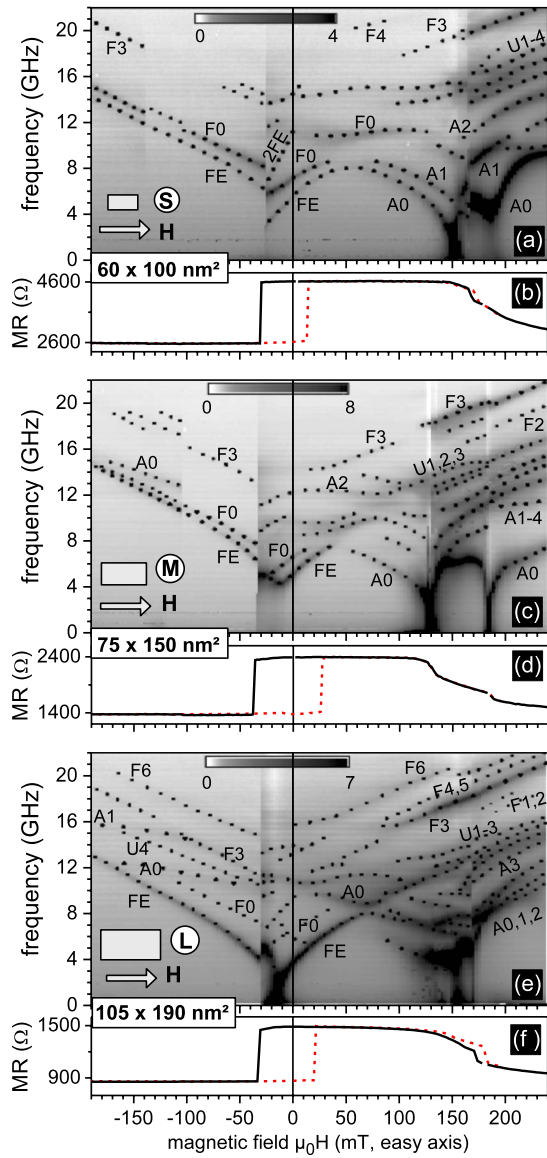
FIG. 2. (Color online) Power spectrum density (log scale, dB) versus descending (SF→AP→P) easy-axis applied field for a device of (a) size S, (c) size M, and (e) size L. Panels (b), (d), and (f): corresponding hysteresis loops.
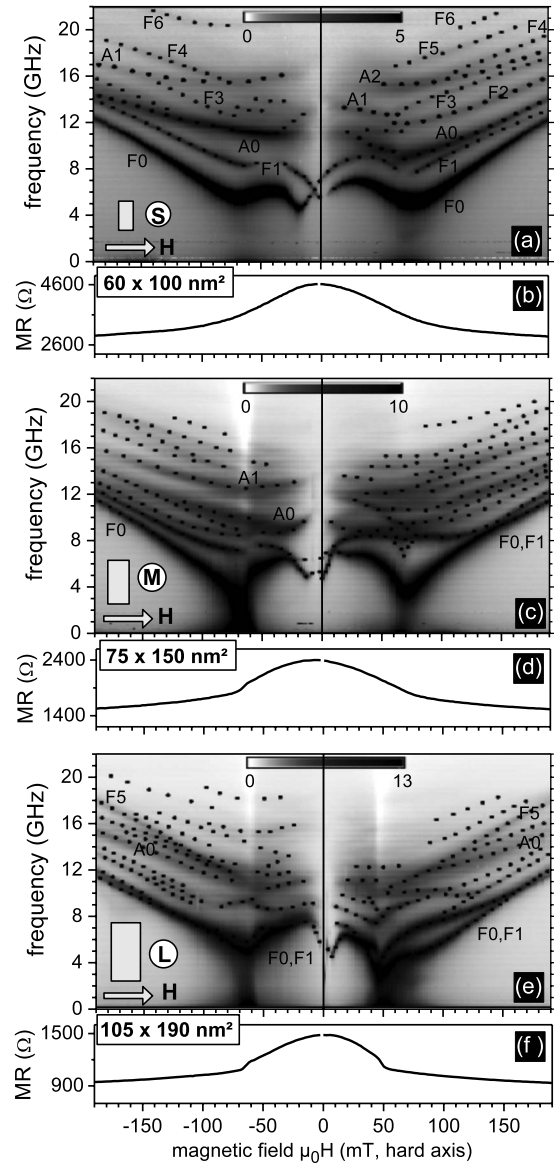
FIG. 3. Power spectrum density (log scale, dB) versus (ascending) hard-axis field for the same devices as in Fig. 2: (a) size S, (c) size M, and (e) size L. Panels (b), (d), and (f): corresponding hysteresis loops.

magnetization and the SAF. With increasing pillar size, this coupling is decreasing while for size S, the shift is 5–11 mT, it is only 3–7 mT for size M, and 1–5 mT for size L.

The bell shape of the HA hysteresis loops (Fig. 3) is consistent with the antiparallel coupling observed on the EA. At zero HA applied field, the devices are always in the AP state. With increasing (absolute value of the) field, the resistance decreases continuously from the maximum resistance of the AP state down to almost parallel remanence, as the magnetizations of the free layer and finally the two SAF layers progressively tilt toward the applied field. Ascending and descending field branch of the HA loops are for most devices identical. In contrast, in the absence of coupling between free layer and SAF, the pillar relaxes with equal probability into P state or AP state when the HA field is switched off, resulting in two branches of the hysteresis loop [see Fig. 1(d)]. Finally,

note that the sharp bends in the resistance curve at about ±60 mT in the measured HA loop for pillar size L, and also present in the calculated HA loop, become more and more rounded for decreasing pillar size, i.e., for increasing antiparallel coupling.

We have used the intrinsic symmetry of the HA loops to align the external field with the symmetry axes of the rectangle by choosing the field direction such that the loops showed highest possible symmetry. For some devices, the loops were, though symmetric at high fields, noticeably asymmetric at low fields; in these cases we have cross checked the alignment with the symmetry of the corresponding HA spectra. The misalignment of the field should therefore not exceed 2°.

B. Setup and experimental methods

To obtain their spin-wave spectra the devices were inserted into a high-bandwidth circuit similar to that in Ref. 21, and their voltage-noise power spectrum density (PSD) was measured for moderate dc bias currents as a function of the applied magnetic field. The noise spectrum at each field step was obtained by subtracting from the spectrum for nonzero bias current a zero-current reference spectrum in order to eliminate noise of nonmagnetic origin. In panels (a), (c), and (e) of Figs. 2 and 3 examples of two-dimensional density plots of the PSD versus the magnetic field are shown, where the dark regions correspond to maxima in the PSD and therefore to eigenexcitations of the magnetic system,[22] i.e., spin-wave modes. The spectra are displayed in a contrast scaling with the logarithm of the noise in excess to the noise at zero current. As the difference in amplitude between the most intense and the weakest modes is even on a logarithmic scale still large, in all figures the gray scale of the PSD has been modulated and black dots have been superimposed to better evidence the weaker modes.

Bias currents used to measure the spectra were chosen as low as possible in order not to affect the mode frequencies but still high enough to obtain sufficient signal-to-noise ratio. Devices of pillar size S were therefore mostly measured at ± 0.1 mA, those of size M at ± 0.2 mA, and those of size L at ± 0.3 mA. The differences in amplitude for opposite current polarity were hardly noticeable on the logarithmic scale, and the maximum difference in the mode frequencies, observed for 0.3 mA, was 0.15 GHz. These observations are in agreement with previous works[23] on similar samples, where a spin-torque threshold current of 1.6 mA for size-L devices has been determined. On the frequency scales considered in this paper, the bias-current dependence of the spectra can therefore be neglected.

Note that electrical-noise measurement techniques allow to detect the spin waves in individual pillars, in contrast to the Brillouin light scattering used for the pseudospin valves in Refs. 11 and 13, where the measured spectra were an average over a large number of devices. Moreover, as no optical or any other direct access to the magnetic layers is needed, the pillars can be measured in their natural working environment, i.e., as the stack actually used in a functional device and subject to electrical currents. Finally, since the magnetoresistance is a function of the relative orientation of the magnetizations in the FL and the RL, these techniques are equally sensitive to spin waves in both the FL and the RL.

III. EXPERIMENTAL RESULTS

In this section, we describe the characteristics of the spectra measured for easy-axis and hard-axis applied fields as well as their dependence on the pillar size. Note that there is no device possessing simultaneously on EA and HA, all the properties stated as typical of a particular pillar size. The properties described in the text are therefore those observed on a majority of the EA spectra and a majority of the HA spectra but not always for the same devices. For the basic identification of the observed spin-wave modes, we recall in Figs. 1(a) and 1(c) the mode dispersion in macrospin approximation for a nanopillar consisting of a SAF and an ideal free layer (i.e., the latter is assumed not to interact with the SAF). EA and HA spectrum each contain two types of modes: the uniform FL modes and the uniform acoustic mode of the SAF. The acoustic SAF mode is thereby the lower of the two SAF eigenmodes and corresponds to oscillations, for which the in-plane components of the SAF layer magnetizations stay antiparallel, i.e., the dynamical magnetizations oscillate 180° out-of-phase. The high-frequency second eigenmode of the SAF, the optical mode (in-plane components of dynamical magnetizations in-phase), is not detected in the measured frequency range up to 26 GHz, and will therefore not be mentioned further.

A. Eigenexcitations for easy-axis applied field

1. Size-independent properties

For all pillar sizes, EA spectra (Fig. 2) contain two groups of modes. The first group consists of V-shaped modes basically symmetric about zero field for high positive and negative fields and history dependent in the hysteretic field region with a discontinuity at the coercive field. Since this is the typical behavior of FL modes [Figs. 1(a) and 1(b)], the modes in this group are labeled with F. The second-mode group consists of modes having a minimum at or near the spin-flop field of the SAF. This being the characteristics of the acoustic modes of the SAF [Figs. 1(a) and 1(b)], the modes in this group are labeled with A. Modes that cannot be assigned unambiguously to one of the groups are labeled with U (like unidentified). Within each group, the modes are numbered consecutively with increasing frequency. The lowest FL mode FE has been labeled differently, because it shows in several aspects a qualitatively different behavior than the next-higher mode F0. As we shall see in the following sections, there is evidence that it might belong to excitations localized near the layer edges (hence the second label E). Occasionally, second harmonics, such as the mode 2FE in Fig. 2(a), are observed.

There are three FL modes common to all pillar sizes: the modes F0 and FE, visible in the P and low-field AP state, and—with a size invariant spacing of 5–6 GHz to F0—the mode F3, mainly visible at high fields.

In the SF region at high positive fields, several SAF modes are observed, the intense lowest modes having either one single minimum [Fig. 2(e)] or two minima at different fields [Figs. 2(a) and 2(c)]. The minima are always positioned in the vicinity of significant changes in the slope of the resistance in the hysteresis loop. The occurrence of more than one such slope change clearly indicates that the magnetization of the reference layer does not undergo a single abrupt transition as associated with the SF but that there are several domains with different transition fields. Independent of the number of observed minima at the SF, the SAF modes show complicated, irregular structures, indicating strong nonuniformities of the SAF layer magnetizations in this field region, and will therefore not be discussed in more detail.

The modes after the SF, which are labeled with U, comprise the lowest FL modes and higher-order SAF modes.

They cannot be identified with certainty because both mode types have similar frequency, slope, and intensity in this field region. Moreover, above the SF, the large angle between the FL magnetization and the RL magnetization boosts the experimental sensitivity to both FL and SAF modes (see Sec. V B) causing, in particular, for sizes S and M abrupt changes in the mode intensity, such that FL modes suddenly appearing above the SF field may be misinterpreted as SAF modes.

For some devices, a change in mode intensity is also observed at a high negative field value [cf. F0, F3 in Fig. 2(a) at −140 mT or A0 in Fig. 2(c) at −105 mT], at which the resistance changes by 10–20 Ω [not visible on the scale of Figs. 2(b) and 2(d)]. The reason for this is a change in the micromagnetic configuration, very likely of the RL (see Sec. V B).

Finally, in the AP state, gaps with pillar size-dependent opening from 2 to 0.5 GHz are observed in the modes FE and, if visible, F0 [see, e.g., Figs. 2(e) and 2(a)]. We will see that this is a consequence of the mutual dipolar coupling between the FL and the SAF leading to anticrossing of FL and SAF modes.

2. Size-dependent properties

In the following, we describe the size-specific properties of the EA spectra. We will see that with increasing pillar size, the spectra undergo characteristic changes, some of which are caused directly by the increasing dimensions while others are most likely consequences of an increasing nonuniformity of the magnetization.

a. Size S. In the EA spectra of the smallest pillars [Fig. 2(a)], the modes FE, F0, and F3 are mostly the only observed FL modes. The opening of the anticrossing gap in F0 is typically 2 GHz. F3 has for all devices a frequency of 22–23 GHz at +240 mT. FE and F0 show a slightly larger device-to-device variation. For some devices, the mode FE is visible up to very high negative fields [as in Fig. 2(a)] with a roughly constant spacing to F0 of about 1.5 GHz, for others it is observed in the low-field region only where the resistance departs from its saturation value, i.e., where the (FL) magnetization shows signs of increasing nonuniformity; in this case, FE rapidly approaches F0 for increasing field and vanishes, once the resistance has reached its saturation value. This correlation of FE to the nonuniformity of the static magnetization suggests that FE might be an edge mode. Another observation in favor of this supposition is that the mode FE has a noticeably higher slope than F0 (due to its tendency to approach F0 asymptotically from below), which would not be the case if both modes were volume modes. The average frequency of F0 is about 16 GHz at −190 mT and 6.5 GHz at zero field.

b. Size M. The EA spectra of devices of pillar size M [Fig. 2(c)] differ from those of the size-S devices in the following points. The mode FE has developed a minimum at low fields, which for some devices may almost reach zero frequency. This effect is likely to be caused by the increased nonuniformity of the magnetization in this field region. Occasionally, the mode F0, too, becomes deformed, though much less than FE. The relative intensity of F0 typically decreases whereas that of FE increases. The observed evolution of FE with the pillar size, too, corroborates the assumption that this mode might be an edge mode. The frequencies of all modes decrease typically by 1 or 2 GHz at high fields. The gap opening in the modes FE and F0 has decreased to 1–1.5 GHz. At very high fields, additional modes, most likely belonging to the FL, appear just above or below the mode F3.

c. Size L. For the size-L devices [Fig. 2(e)], the gap opening in the mode FE does not exceed 0.5–1 GHz, and the frequencies of FE and F3 have decreased by another gigahertz. The spacing between FE and F3 has not changed with respect to size M or S. Above F3, three additional FL modes (F4 to F6) with a spacing of 1 GHz, and below F3 two extremely weak modes (F1, F2) have appeared. As for size M, the mode FE is strongly deformed in the low-field region and has still gained intensity with respect to F0.

B. Eigenexcitations for hard-axis applied field

1. Size-independent properties

In Fig. 3 are depicted the HA spectra of the same devices as in Fig. 2. The FL modes have a characteristic W shape with two minima in the lowest modes at about ±70 mT. Though 70 mT is for all pillar sizes substantially higher than the measured anisotropy fields, the minima are often[24] interpreted as to correspond to the saturation of the free-layer magnetization along the HA [cf. also Figs. 1(c) and 1(d)].

At or near zero field, the modes F0 and F1 show typically one, sometimes two sharp minima, which become deeper with increasing pillar size, and which are not present in the macrospin HA spectrum [Fig. 1(c)]. We therefore suspect that at least one of the modes observed at low fields is actually an edge mode FE. As a matter of fact, if at zero EA field, the lowest mode is—as we think—an edge mode, then the lowest mode at zero HA field must be an edge mode, too because zero EA and zero HA field are formally identical. The observed field dependence of the frequency of the mode F0 then implies that its character must be changing (continuously) from edge mode at low fields to volume mode at high fields. Such a progressive change in the mode character would be consistent with the expected saturation process of the magnetization along the HA; for very low HA field, the magnetization in the central part of the layer is aligned along the EA due to the shape anisotropy, and only in narrow zones along the short edges of the rectangle, the magnetization starts to align with the HA. For increasing field, these edge zones (domains) expand continuously toward the layer center, until for some field value the volume magnetization and finally the magnetization in the zones along the long edges of the layer saturate along the HA. The oscillations of this increasing part of the magnetization parallel to the field would obviously correspond to edge modes at low fields, and to volume modes at high fields; for intermediate field values, they would have a mixed character.

Finally, for most devices, we also observe the almost horizontal lowest acoustic modes of the SAF, A0 and A1 [see, e.g., Fig. 3(a)], where A0 has a frequency of typically 10–12

GHz at zero field. Note that, in particular, for size-S devices, the SAF modes are strongly asymmetric w.r.t. zero field, even though the FL modes and the hysteresis loop are basically symmetric. As will be shown in Sec. VI, this asymmetry cannot be explained by a misalignment of the external field with the HA.

2. Size-dependent properties

a. Size S. The HA spectra of size-S devices are characterized by rounded saturation minima of the FL modes at ±70 mT [cf. Fig. 3(a)]. The frequency minima of the mode F0 are thereby not zero but raised to values between 4 and 6 GHz, which is a consequence of the mutual dipolar coupling between the FL and the SAF, as we shall see in Sec. VII. Typically 5–7 FL modes, F0 to F6 in Fig. 3(a), are observed, where the first two modes have frequencies of 12 GHz and 14 GHz, respectively, at ±190 mT. The lowest mode F0 has much higher intensity than the other modes, and its frequency at high fields is the same for all measured devices of size S. The frequencies of the higher modes slightly vary from device to device. [In Fig. 3(a), the modes F2 and A1 seem to accidently coincide at positive fields; however, for other devices, F2 is clearly resolved.] The presence of F1 and F2 in the HA spectra for several devices of size S with rather high intensity is of great importance because at least the mode F2 is not observed in the EA spectra, not even after the SF where the experimental sensitivity is comparable to that on the HA (see Sec. V B).

b. Size M. In the spectra of pillar size M [Fig. 3(c)], the saturation minima at ±70 mT in the mode F0 are much deeper than for size S, which is consistent with the lower dipolar coupling between the FL and the SAF concluded from the EA hysteresis loops and spectra (see also Sec. VII). The minima at zero field are considerably sharper than for size S indicating increasing importance of edge-domain effects. The acoustic SAF modes have with about 10 GHz at zero field for A0 a slightly lower frequency than for size S, which is either due to a smaller interlayer exchange or the increasing nonuniformity of the SAF layer magnetizations (resulting, e.g., on the EA in the observed stepwise switching in the SF region). Finally, the overall mode spacing has noticeably decreased compared to size S, as should be expected.

c. Size L. In the spectra of pillar size L [Fig. 3(e)], the minima in the modes F0 and F1 at ±70 mT reach, as for size M, markedly lower frequencies than for size S. Both F0 and F1 are strongly deformed in the vicinity of their minima and may even cross each other. The minimum at zero field has still become slightly deeper, the impact of edge domains now being dominant. Contrary to size S, the shape of the modes in the low- and medium-field region is strongly device dependent and sensitive to small changes in the field direction.

IV. OUTCOMES AND LIMITS OF THE MACROSPIN MODEL

Before making a detailed and rigorous analysis of the field dependence of the modes frequencies in the next sec-

tion, we start by attempting to model the free-layer modes F0 using conventional Kittel fits. The aim is twofold: motivate the need for a more elaborate analysis by showing quantitative and qualitative limits of the macrospin approximation, and obtain approximate starting values for the magnetizations.

Approximating the free layer as an isolated rectangular platelet with only shape anisotropy, its ferromagnetic resonance frequency is described by the well-known Kittel law, which for EA applied field (x direction) reads

$$\omega^2 = \gamma_0^2 [H^{appl} + H_k][H^{appl} + (N^z - N^x)M_S]$$

and for HA field (y direction),

$$\omega^2 = \gamma_0^2 [H^{appl} - H_k][H^{appl} + (N^z - N^y)M_S],$$

where M_S is the saturation magnetization of the free layer and $H_k = (N^y - N^x)M_S$ the in-plane shape anisotropy field.

Applying Kittel fits to the modes F0 in the high-field regions of the spectra in Figs. 2 and 3, allows us to extract M_S and H_k for the different pillar sizes, independently for EA and HA. Using the demagnetizing factors N^x, N^y, and N^z of Ref. 19, we obtain from the modes F0 in the EA spectra the following values for M_S and H_k: for size S $\mu_0 M_S = 1.14$ T (for most devices of size S ≈ 1.25 T) and $\mu_0 H_k = 37$ mT, for size M $\mu_0 M_S = 1.04$ T and $\mu_0 H_k = 35$ mT, and for size L $\mu_0 M_S = 0.91$ T and $\mu_0 H_k = 30$ mT. In comparison, for the modes FE, larger magnetizations (1.3–1.1 T) but much smaller anisotropy fields (less than 12 mT) are obtained. Similarly, the modes F0 on the HA yield for size S $\mu_0 M_S = 1.41$ T and $\mu_0 H_k = 55$ mT (universal for size S), for size M $\mu_0 M_S = 1.40$ T and $\mu_0 H_k = 76$ mT, and for size L $\mu_0 M_S = 1.41$ T and $\mu_0 H_k = 78$ mT.

The minimum requirement for these values to be reasonable approximations is that the magnetizations and shape anisotropy fields extracted from EA and HA spectrum of the same device are roughly equal. However, as can be seen, both M_S and H_k are considerably larger on the HA, the discrepancies becoming larger with increasing pillar size. In addition, on the HA—and, if the mode FE is used, also on the EA—the anisotropy fields are neither consistent with the extracted magnetization nor with the anisotropies found by astroid measurements[19] (cf. Sec. II). Therefore, treating the free layer and the SAF as uncoupled systems consisting of uniformly magnetized layers is obviously insufficient to describe the eigenexcitations of nanopillars. The next section will be dedicated to a rigorous treatment of spin waves in a coupled three-layer system with lateral confinement.

V. MODEL OF SPIN-WAVE MODES IN NANOPILLARS

A. Dipolar-exchange spin waves with quantized wave vectors

1. Eigenexcitations of coupled three-layer system

An MTJ nanopillar consists basically of three confined magnetic layers: the free layer, which will be labeled with the index "F," and below the two SAF layers—the reference (top) layer and the pinned (bottom) layer—labeled with indices "1" and "2," respectively. The magnetization dynamics

in each layer $l \in \{F, 1, 2\}$ of this coupled three-layer system is governed by the Landau-Lifshitz equation.

For small amplitude precessions, the magnetization $\vec{M}_l(\vec{r}, t)$ can be decomposed in zeroth-order approximation into a time independent uniform (U) equilibrium component $\vec{M}_l^U$ (saturation magnetization M_l) and a small perpendicular dynamical part $\delta \vec{M}_l^U(\vec{r}, t)$. Static nonuniformities of the equilibrium magnetization will be discussed in Sec. V B. The dynamical component $\delta \vec{M}_l^U(\vec{r}, t)$ can be approximated as a sum of plane spin waves,

$$\delta \vec{M}_l^U(\vec{r}, t) = \mathfrak{R} \sum_{\vec{k}} \delta \vec{M}_l^U(\vec{k}) e^{i\vec{k}\vec{r} - i\omega_{\vec{k}}t}, \qquad (1)$$

where the wave vectors $\vec{k} = (k_x, k_y, 0)$ of the partial waves are quantized due to the spatial confinement of the layers. The out-of-plane component k_z is zero for all modes in the experimental scope due to the very small layer thicknesses of 2–3 nm. The quantization of the in-plane components k_x, k_y will be discussed in detail later on. The frequencies $\omega_{\vec{k}}$ of the partial waves are the eigenfrequencies of the three-layer system.

In the effective fields acting on the magnetizations, the following interactions have been taken into account: the applied field $\vec{H}^{appl}$, the exchange-bias field acting on the bottom layer of the SAF (coupling constant J^{eb}), the interlayer exchange coupling of the SAF layers (coupling constant J^{int}), and the (intralayer) exchange interaction in each layer (exchange stiffness constant A_l), as well as the demagnetizing fields and mutual dipolar coupling of the layers. For the demagnetizing fields, we use the standard tensor expression for uniformly magnetized ellipsoidal bodies, where the diagonal components of the diagonal (self-) demagnetizing tensors $\mathbf{N}_l$ are the demagnetizing factors N_l^x, N_l^y, and N_l^z of the rectangular layers. Although this approximation is expected to be satisfying for the static demagnetizing field, it is rather crude for the dynamical part since the dynamical magnetization is nonuniform unless $\vec{k} = 0$.

The fields resulting from mutual dipolar coupling are given by analogous expressions where the (self-)demagnetizing tensors of trace 1 are replaced by the mutual demagnetizing tensors[25] $\mathbf{N}_{ml}$ of trace 0 ($l, m \in \{F, 1, 2\}$, $l \neq m$). For the given pillar geometry, $\mathbf{N}_{ml}$ is diagonal, too, as can easily be shown using the formulas for the tensor components in Ref. 25. The diagonal components will be referred to as the mutual dipolar coupling constants N_{ml}^x, N_{ml}^y, and N_{ml}^z.

Note that there is no significant perpendicular surface anisotropy at the top and the bottom surfaces of the layers in MTJs, as has been demonstrated in Refs. 19 and 26. Since the impact of the bias current on the experimental spectra has been found to be negligible, we do not include current-based interactions, such as spin torque or the Oersted field. The latter does, e.g., not exceed 1 mT for a current of 0.3 mA and an impact diameter of 100 nm.

With these approximations, the Landau-Lifshitz equations of the three pillar layers become a system of $3 \times 3 = 9$ coupled linear equations for the components of the dynamical magnetizations $\delta \vec{M}_l^U(\vec{k})$. It can be solved as the eigen-

value problem of the 9×9 coefficient matrix $\mathbf{F}$ of the nine-component vector $[\delta \vec{M}_F^U(\vec{k}), \delta \vec{M}_1^U(\vec{k}), \delta \vec{M}_2^U(\vec{k})]$ describing the dynamics of the three-layer system as a whole. The eigenvalues of $\mathbf{F}$ are the eigenexcitations $\omega_{\vec{k}}$ of the three-layer system and can be calculated numerically as a function of the applied field, yielding the expected spin-wave spectra $\omega_{\vec{k}}(H^{appl})$ of the nanopillar.

2. Quantization of in-plane wave vector

The in-plane components k_x, k_y of the wave vector are determined by the boundary conditions (BCs) imposed on the dynamical magnetization [Eq. (1)] at the lateral layer boundaries $x = \pm L_x/2$ and $y = \pm L_y/2$. For simplicity, we will consider the x component (along the long edge of the rectangle) as an example, where any of the following statements hold equally for the y component with x and y permuted.

For the x component, the BC reads

$$\left[\frac{\partial}{\partial \xi_x} \delta \vec{M}_l^U(\xi_x, \xi_y) \pm d_x^\pm \delta \vec{M}_l^U(\xi_x, \xi_y) \right]_{\xi_x = \pm 1/2} = 0, \qquad (2)$$

where $\xi_x = x/L_x$. Equation (2) is a modified version of the effective BC derived by Guslienko *et al.*[9] for thin magnetic stripes. In difference to Ref. 9, we allow for different pinning parameters d_x^+ and d_x^- at opposite boundaries $x = \pm L_x/2$ to account for potential asymmetries in the pinning expected from a real device. Moreover, instead of using the analytical expression (5) in Ref. 9 to calculate the (dimensionless) pinning parameters, we will extract approximate values for $d_x^\pm$ from the experimental spectra (see Secs. VI and VII).

Applying the BC [Eq. (2)] to the sinusoidal mode profile,

$$\mathfrak{R} e^{i\vec{k}\vec{r}} = \sin(k_x x + \phi_x)\sin(k_y y + \phi_y), \qquad (3)$$

of the partial spin waves in $\delta \vec{M}_l^U$ [Eq. (1)] yields for the wave-vector component k_x and the phase ϕ_x the quantization conditions,

$$\mp k_x L_x \cot\left(\pm k_x \frac{L_x}{2} + \phi_x \right) = d_x^\pm. \qquad (4)$$

It is convenient to express $k_x L_x$ in the argument of the cotangent as multiples of π, thus defining the—in general, nonintegral—mode numbers,

$$n_x = \frac{k_x L_x}{\pi} \qquad (5)$$

of the quantized spin-wave modes (n_x, n_y).

For symmetric pinning, $d_x^+ = d_x^- = d_x$, it follows from Eq. (4) that the cotangent has to be antisymmetric, yielding $\phi_x^s = \pi/2$ or $\phi_x^a = 0$, i.e., symmetric or antisymmetric wave functions [Eq. (3)]. In the limiting case of totally unpinned BC, $d_x = 0$, the mode numbers n_x^0 are integers, starting at 0, and the corresponding wave functions alter between symmetric and antisymmetric for successive mode numbers, starting with symmetric, such that there are always antinodes at both boundaries.

For finite values $d_x > 0$ of the pinning, the mode numbers n_x are no longer integers. Plotting n_x versus d_x by means of Eqs. (4) and (5) shows that with increasing d_x, the deviations

Δn_x of n_x from the corresponding integral values n_x^0 of the unpinned case increase continuously from $\Delta n_x = 0$ for $d_x = 0$ (unpinned) to $\Delta n_x = 1$ for $d_x = \infty$ (totally pinned). Therefore, the mode numbers for total pinning, $n_x^\infty = n_x^0 + 1$, are integers again. For a fixed intermediate value d_x, the deviation Δn_x of the mode number n_x from the corresponding integral mode number n_x^0 is found to rapidly decrease with increasing n_x^0. For a given pinning, the mode numbers are therefore no independent variables once one mode number (e.g., that of the lowest mode) has been fixed, all other mode numbers are fixed, too.

In case of slightly asymmetric pinning, $d_x^+ \neq d_x^-$, the phase ϕ_x differs from the values $\phi_x^{s,a}$ by a small phase shift $\Delta\phi_x$, such that the wave functions are no longer totally symmetric or antisymmetric. In this case, the mode numbers n_x are necessarily nonintegral. In the hypothetic case of totally asymmetric pinning, $d_x^+ = 0$ and $d_x^- = \infty$ (or vice versa), $\Delta n_x = 0.5$ and $\Delta\phi_x = \Delta\phi_x^{\max} = \pi/4$. For arbitrary pinning, $\Delta\phi_x$ is an unknown function of $d_x^\pm$ and n_x.

The pinning for a given in-plane direction of a magnetic element depends on its dimensions and in addition on the inhomogeneity of the internal field.[4,9,27] Consequently, the mode numbers are expected to be larger for the x direction than for the y direction of the same pillar, and possibly different for easy-axis and hard-axis applied field.

B. Expected experimental sensitivity

1. Formulation of the problem

As described in Sec. II, the experimental spin-wave spectra are obtained by measuring the voltage noise of the pillar. To be more precise, we measure the average of the local voltage noise over the pillar area. The local voltage noise is the product of the local current density and the local magnetoresistance (MR) noise generated by spin waves in the FL and the RL. In the ideal case of a homogeneous in-plane distribution of the current, the measured voltage noise is proportional to the average of the local MR noise. For the sake of simplicity, we will derive the expected MR noise for excitations in the FL, where the analogous expressions for the RL are obtained by permuting the indices F and 1. The consequences of inhomogeneities will be discussed later in this section.

The MR noise signature of a partial spin wave with wave vector $\vec{k}$ representing the FL mode (n_x, n_y) is in linear order given by the square of

$$\delta R_F(\vec{k}) = \frac{1}{S_{pil}} \int_{S_{pil}} \vec{M}_1(\vec{r}) \cdot \delta\vec{M}_F^U(\vec{k}) \, \Re e^{i\vec{k}\vec{r}} d\vec{r}, \quad (6)$$

where S_{pil} is the pillar area, $\vec{M}_1(\vec{r})$ the micromagnetic equilibrium magnetization of the RL, $\delta\vec{M}_F^U(\vec{k})$ the amplitude vector, and $\Re e^{i\vec{k}\vec{r}}$ the spatial dependence (wave function) of the spin wave in the FL [cf. Eq. (1)]. Decomposing $\vec{M}_1(\vec{r})$ as before into a uniform macrospin component $\vec{M}_1^U$, dominating in the central (volume) part of the layer, and the remaining $\vec{r}$-dependent edge-domain components $\delta\vec{M}_1^E(\vec{r})$, yields as final expression for the MR variation (6),

TABLE I. Dependence of the magnetoresistance noise [Eq. (7)] on the static micromagnetic configuration of layer $l \in \{F, 1\}$ and the mode character. (a) Leading-order contributions of volume magnetization, $M_l^V(\theta)$ and edge-domain contributions, $\overline{\delta M_l^E}(n_x, n_y, \phi_x, \phi_y, \theta)$, versus easy-axis and hard-axis applied field in different field regions. δ_{lm} is the Kronecker symbol. (b) Leading-order terms of integral $\overline{W}_x(n_x, \phi_x)$ of the wave function versus the mode number $n_x = n_x^0 + \Delta n_x$ in the regime of weak and strong pinning. $\overline{W}_y$ is given by analogous expressions.

(a)

Field region		$M_l^V(\theta)$	$\overline{\delta M_l^E}$
Easy axis			
Below second SF	$H < H_{SF2}$	$M_l \sin\theta_0$	
P state	High H	$M_l \Delta\theta$	
	Low H	$M_l \Delta\theta$	$\overline{\delta M_l^E}$
AP state	Low H	$M_l \Delta\theta$	$\overline{\delta M_F^E}\delta_{lF}$
	High H	$M_l \Delta\theta$	$\overline{\delta M_1^E}\delta_{l1}$
Above SF	$H > H_{SF}$	$M_l \sin\theta_0$	
Hard axis			
	$|H| > 0$	$M_l \sin\theta_0$	
	$H \approx 0$	$M_l \Delta\theta$	$\overline{\delta M_l^E}$

(b)

Mode number n_x^0	Integral $\overline{W}_x(n_x, \phi_x)$	
	For weak pinning ($\Delta n_x \ll 1$)	For strong pinning ($\Delta n_x \approx 1$)
0	1	$2/\pi$
Odd	$\Delta\phi_x/n_x \cdot 2/\pi$	$\Delta\phi_x(1 - \Delta n_x)/n_x$
Even	$\Delta n_x/n_x$	$1/n_x \cdot 2/\pi$

$$\delta R_F(n_x, n_y, \phi_x, \phi_y, \theta) = \delta M_F^U(\vec{k})[M_1^V(\theta)\overline{W}_x(n_x, \phi_x)\overline{W}_y(n_y, \phi_y)$$
$$+ \overline{\delta M_l^E}(n_x, n_y, \phi_x, \phi_y, \theta)]. \quad (7)$$

The first term, $M_1^V \overline{W}_x \overline{W}_y$, is the contribution of the uniform volume magnetization to the MR noise (hence the superscript V). $M_1^V(\theta) = \sin\theta M_1$ is the projection of $\vec{M}_1^U$ onto $\delta\vec{M}_F^U(\vec{k})$, where θ denotes the angle between the macrospins of FL and RL. $\overline{W}_x$ and $\overline{W}_y$ are the integrals of the x- and y-dependent factors of the wave function [Eq. (3)], respectively.

The second term, $\overline{\delta M_1^E}$, is the contribution of the static edge-domain magnetization components of the RL to the noise signature of the (volume) FL mode (n_x, n_y) (not to be confused with edge modes). It is the spatial average of the projection of $\delta\vec{M}_1^E(\vec{r})$ onto $\delta\vec{M}_F^U(\vec{k})$ weighted by the wave function [Eq. (3)].

Mathematical expressions for $\overline{W}_x(\overline{W}_y)$ and $\overline{\delta M_1^E}$ as well as details on the derivation of Eq. (7) can be found in Appendix A. For the following discussion, it is sufficient to consider the leading-order terms of these quantities listed in Table I.

The terms M_1^V and $\overline{\delta M_1^E}$, resulting from the equilibrium magnetization, obviously depend on the static micromagnetic

configuration of the pillar layers. The quantities $\bar{W}_x$, $\bar{W}_y$, and again $\overline{\delta M_1^E}$, involving the wave function, depend on the symmetry properties of the spin-wave mode. In the following, we will show which modes are expected to be observed in the experimental spectra under which conditions by analyzing the micromagnetic configuration and mode character dependence of the experimental sensitivity.

2. Micromagnetic configuration dependence of sensitivity

The micromagnetic configuration of the pillar is sensitive to direction and strength of the external field, which is why in the following we distinguish between easy-axis and hard-axis applied field and identify field regions of distinct values M_l^V and $\overline{\delta M_l^E}$ ($l \in \{F, 1\}$).

The largest contributions to the MR noise and hence highest sensitivity are expected in the field regions of maximum volume magnetization contributions $M_l^V(\theta)$, i.e., where $\sin \theta \gg 0$. As can be seen from Table I(a), a large zeroth-order term $\sin \theta_0$ is found for nonzero HA fields, above the SF at positive EA fields and below the SF at negative EA fields. In the AP and the P state, $\sin \theta_0 = 0$, such that the leading-order terms are of first order in $\Delta \theta$. θ_0 thereby denotes the angle between the FL and the RL macrospins in case of an ideal pillar, and $\Delta \theta$ a small deviation of θ from θ_0 caused by a misalignment of the exchange-bias field or the external field with the symmetry axes of the layers.

The presence of edge domains on the EA, as marked in Table I(a), can be deduced from the hysteresis loops, as is explained in detail in Appendix A 1. Whether these edge domains give nonzero contributions $\overline{\delta M_l^E}$ to the MR noise depends on the symmetry properties of both the micromagnetic state and the wave functions (see Appendix A 2 for details).

In summary, high sensitivity to both FL and SAF modes can be expected on the HA at any finite field value and on the EA above the SF at positive fields. Weak higher modes will therefore be visible, if at all, in these field regions (cf. Figs. 2 and 3). The sensitivity below the SF at negative EA fields is also enhanced, though substantially less than for the other two cases. The change in intensity can be nicely seen in Fig. 2(a) at −140 mT, and in Fig. 2(c) at −105 mT.

For EA fields between the two SF fields, i.e., in AP and P state, modes become visible only through the misalignment $\Delta \theta$ of the macrospins or through edge domains of appropriate symmetry. From the latter, slightly increased sensitivity is expected for FL modes in the AP state at high positive fields just below the SF, and for both FL and SAF modes at low fields in P and AP states. The presence of edge domains may thereby entail the appearance of the corresponding edge modes in the spectra.

3. Mode character dependence of sensitivity

The quantities $\bar{W}_x$, $\bar{W}_y$, and $\overline{\delta M_1^E}$ depend on the symmetry properties of the wave function of the mode (n_x, n_y). As the edge-domain contributions become effective mainly in the low-field region, in which our model is in any case not expected to be accurate, we consider only the integrals $\bar{W}_x$ and

$\bar{W}_y$ belonging to the volume magnetization contribution M_l^V, dominating at high fields.

In Table I(b) the leading-order terms of $\bar{W}_x$ are listed as a function of the mode number $n_x = n_x^0 + \Delta n_x$ in the regime of weak and strong pinning. n_x^0, Δn_x, and $\Delta \phi_x$ are thereby defined as in Sec. V A. The y-dependent factor $\bar{W}_y$ is given by analogous expressions.

For zero pinning ($\Delta n_x = \Delta \phi_x = 0$), the fundamental mode $n_x^0 = 0$ is the only visible mode. In the presence of pinning, the higher modes $n_x^0 \geq 1$ begin to appear: for symmetric pinning ($\Delta n_x > 0$, $\Delta \phi_x = 0$) only those with symmetric wave functions (even n_x^0), in case of asymmetric pinning ($\Delta n_x > 0$, $\Delta \phi_x \neq 0$) also those with antisymmetric wave functions (odd n_x^0).

For weak pinning ($\Delta n_x \ll 1$), $\bar{W}_x$ is for all higher modes $n_x^0 \geq 1$ of first order in a small quantity: in Δn_x for even n_x^0, in $\Delta \phi_x$ for odd n_x^0. In Appendix A, we show that the expected intensities of the higher modes $(n_x^0, n_y^0) = (1,0)$, $(0,1)$, and $(2,0)$ are about two orders of magnitude lower than that of the fundamental mode $(n_x^0, n_y^0) = (0,0)$, whereas the mode $(n_x^0, n_y^0) = (1,1)$ is expected to have a four orders of magnitude lower intensity than $(0,0)$.

For strong pinning ($\Delta n_x \approx 1$), the natural reference mode numbers are the mode numbers $n_x^\infty = n_x^0 + 1$ of total pinning: even (odd) n_x^0 in the table correspond to odd (even) n_x^∞. $\bar{W}_x$ for symmetric wave functions (even n_x^0, odd n_x^∞) has now become a zeroth-order quantity like for the lowest mode $n_x^0 = 0 (n_x^\infty = 1)$ whereas for antisymmetric wave functions (odd n_x^0, even n_x^∞), it has become second order in $(1 - \Delta n_x)$ and $\Delta \phi_x$. Consequently, the lowest higher-order modes close to $(n_x^\infty, n_y^\infty) = (3,1)$ and $(1,3)$ will have intensities comparable to that of the fundamental mode $(n_x^\infty, n_y^\infty) = (1,1)$. Modes with an even mode number $n_{x,y}^\infty$ are expected to be at least four orders of magnitude weaker than $(1,1)$.

The above results on the expected relative mode intensity have been obtained under the assumption of homogeneous current density and homogeneous saturation magnetizations. Under these conditions, the voltage noise is proportional to the MR noise, and—at high fields where the edge-domain contributions are negligible—the MR noise is proportional to $(\bar{W}_x \bar{W}_y)^2$. As we have seen, in this case higher modes become visible if the integrals $\bar{W}_x$ and $\bar{W}_y$ are nonzero, that is for nonzero asymmetric pinning. However, even in the absence of pinning, the measured voltage noise can be nonzero, namely, if the saturation magnetization or the current distribution are inhomogeneous because then the average [Eq. (6)] over the pillar area becomes an integral of a generally unharmonic—and for asymmetric inhomogeneities also asymmetric—function. For real devices, we may therefore expect finite sensitivity to most of the higher modes.

VI. EXTRACTION OF MATERIAL PARAMETERS

In Sec. V A, we have derived the mode frequencies $\omega_{\vec{k}}$ as a function of the material parameters M_l, A_l, J^{eb}, and J^{int}, and the geometry parameters (L_x, L_y), (N_l^x, N_l^y, N_l^z), and $(N_{ml}^x, N_{ml}^y, N_{ml}^z)$, as well as the mode numbers (n_x, n_y). In this

TABLE II. Material and geometry parameters used to calculate the spectra and hysteresis loops in Fig. 4. Error bars for the parameters are given in the text. The labels *fmn* and *amn* associated to the mode numbers are those in Fig. 4.

Parameter		Extracted value
Saturation magnetization	$\mu_0 M_{F,1}$	1.27 T
	$\mu_0 M_2$	1.4 T
Exchange stiffness	$A_{F,1}$	18.0×10^{-12} J/m
	A_2	14.0×10^{-12} J/m
Exchange bias	J^{eb}	4.5×10^{-4} J/m^2
Interlayer exchange	J^{int}	-3.9×10^{-4} J/m^2
Lateral pillar dimensions	L_x	100 nm
	L_y	60 nm
Demagnetizing factors	(N_F^x, N_F^y, N_F^z)	$(0.035, 0.065, 0.9)$
	$(N_{1,2}^x, N_{1,2}^y, N_{1,2}^z)$	$(0.027, 0.049, 0.924)$
Dipolar coupling constants	$(N_{F1}^x, N_{F1}^y, N_{F1}^z)$	$(0.01, 0.018, -0.028)$
	$(N_{F2}^x, N_{F2}^y, N_{F2}^z)$	$(0.005, 0.009, -0.014)$
	$(N_{12}^x, N_{12}^y, N_{12}^z)$	$(0.007, 0.012, -0.019)$
Mode numbers easy axis	(n_x, n_y)	f00, a00: (0.4,0.0)
		f10, a10: (1.13,0.0)
		f01, a01: (0.4,1.0)
		f20, a20: (2.05,0.0)
		f11, a11: (1.13,1.0)
Mode numbers hard axis	(n_x, n_y)	f00, a00: (0.2,0.0)
		f10, a10: (1.05,0.0)
		f01, a01: (0.2,1.0)
		f20, a20: (2.02,0.0)
		f11, a11: (1.05,1.0)
		f21, a21: (2.02,1.0)

section, we will finally extract these parameters from the experimental spectra. Since the model is based on the assumption of uniform equilibrium magnetizations, its application can be expected to be reasonable only for the smallest pillar size S, for which the nonuniformities of the magnetization had been found to be minimum. Following the experimental evidence, we assume that in the EA spectra, the modes F0 and F3, and in the HA spectra, the modes F0 to F5 and A0, A1 are (at sufficiently high fields) volume modes describable by the model.

As a matter of fact, not all of the above quantities are free input parameters to the model. In Appendix B, we show that on the basis of the measured layer dimensions, basic OOMMF simulations, previous works published in the literature, and a couple of reasonable assumptions, the number of free parameters can be reduced to the following quantities: the three mutual dipolar coupling constants N_{F1}^x, N_{F2}^x, and N_{12}^x; magnetization M_F and exchange stiffness constant A_F of the free layer; interlayer exchange J^{int} and exchange bias J^{eb} of the SAF; the mode numbers of the lowest FL and SAF mode.

Also in Appendix B, we extract minimum and maximum values for the remaining parameters by adjusting the calculated modes and hysteresis loops to the corresponding experimental data [Figs. 2, 3(a), and 3(b)]. In particular, we show that from the experimental constraints, it follows that

the pinning of the magnetization at the boundaries must be weak.

Best overall agreement of experiment and theory is obtained for the parameters in Table II. The calculated spectra and hysteresis loops are shown in Fig. 4. In the following, we will point out similarities as well as differences between experiment and theory, and will discuss the "technical" reliability of the parameter values. The physical consequences are subject of the next section.

The HA spectra [Figs. 3(a) and 4(c)] show quantitative agreement for the FL modes F0 to F3 at medium and high fields, and for the lowest SAF mode A0 at high negative field only. However, there is no calculated mode corresponding to the mode F4; the frequency of the mode f21, which is the next-higher mode after f20/f11, is much too high for F4. A possible reason for this discrepancy might be our for higher modes rather crude approximation of the dynamical demagnetizing field (see below). The systematic asymmetry of the SAF modes, resulting in a much lower frequency of A0 at positive field, cannot be accounted for by a tilting of the field w.r.t. to the HA, as this would affect both FL and SAF modes as well as the hysteresis loop. It might rather be caused by a misalignment of the exchange-bias field, determining the magnetic symmetry axis of the SAF, with the geometrical symmetry axes of the rectangle, coinciding with the mag-
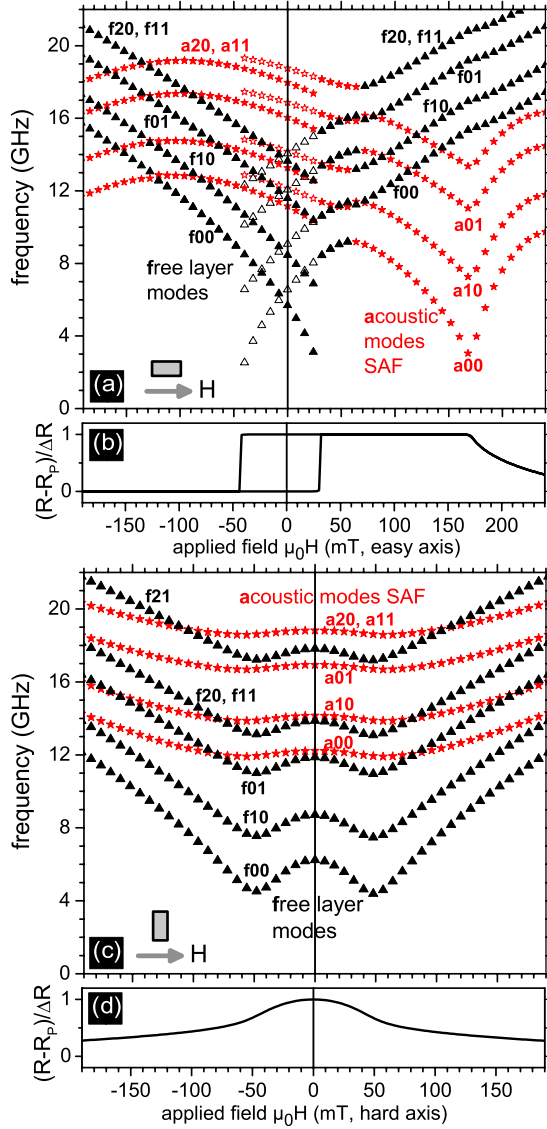
FIG. 4. (Color online) Calculated mode frequencies versus magnetic field along (a) easy axis and (c) hard axis for a pillar of size S. Panels (b) and (d) show the corresponding calculated hysteresis loops. The parameters used to calculate the spectra are given in Table II. The modes f20 and f11 have practically identical frequency, which is why only one mode is displayed. In panel (a), filled symbols are used for ascending field (P→AP→SF) and open symbols for descending field.

netic symmetry axes of the free layer. In the zero-field region, the differences between calculated and experimental HA spectra become substantial, as the measured modes develop pronounced minima whereas the model predicts a local frequency maximum.

On the EA [Figs. 2(a) and 4(a)], the calculated modes f00 and f20/f11 fit the average experimental modes F0 and F3 (see Sec. III A) rather well. In particular, the gap opening in the mode F0 is reproduced in the theoretical spectrum. The modes f01 (F2), and—if none of the unidentified modes U is F1—also f10, are not observed in the experimental EA spectra. Their absence is likely to be due to either an overall lack of intensity, first noticeable for the weakest modes or a lower

sensitivity to these particular modes on the EA, although our considerations in Sec. V B yield no satisfying explanation for the different visibility for EA (above the spin flop) and HA field. For the SAF modes, there can be only qualitative agreement due to the multiple SF in the experiment, which—like the low-frequency supposed edge modes FE—can of course not be described by a macrospin-based model. Finally, the calculated hysteresis loops in Figs. 4(b) and 4(d) are in qualitative agreement with the measured loops.

Main error sources for any of the parameters are obviously the various assumptions in Sec. V A and Appendix B. In particular, our representation of the dynamical demagnetizing field in the standard tensor expression for uniformly magnetized ellipsoidal bodies can be expected to be a reasonable approximation only for the lowest mode because there the dynamical magnetization is indeed almost uniform. As we extract all material parameters except for the exchange stiffnesses from this mode, their values are only little affected by this approximation. Moreover, in small magnetic elements, the exchange interaction is the dominating contribution to the frequencies of the higher modes and not the dipole interaction.

The value of $\mu_0 M_F$ is found to be between 1.25 and 1.3 T, A_F is expected to lie in the interval $(18 \pm 3) \times 10^{-12}$ J/m. Under the assumptions of Appendix B, the same holds true for M_1 and A_1. The error of M_2 and A_2 is significantly larger than for the FL and the RL because of the additional dependence on the thin-film value of the CoFe layer and the ignorance of the experimental exchange bias and the actual SF field. $\mu_0 M_2$ is expected to be contained in the interval (1.4 ± 0.1) T and A_2 in $(16 \pm 4) \times 10^{-12}$ J/m. J^{int} is estimated to be $(-4.0 \pm 0.4) \times 10^{-4}$ J/m^2 and $J^{eb}(4.2 \pm 0.7) \times 10^{-4}$ J/m^2.

The mode numbers of F0 (f00) have to be smaller than (0.6,0.0), or (0.3,0.2) for $n_y > 0$, in order to ensure satisfactory agreement in frequency and a reasonable value for A_F. The agreement is better, if the mode numbers are chosen smaller on the HA than on the EA, and $n_x > n_y$. For the sake of simplicity, we have therefore set $n_y = 0$.

$N_{F1}^x = 0.01$ and $N_{F2}^x = 0.005$ are uniquely determined by the experimental constraints with a maximum deviation of ± 0.002. The deviations of ± 10 nm of the lateral dimensions L_x, L_y from the mean values will change all geometry related parameters accordingly.

VII. DISCUSSION

In the previous sections, we have modeled the spin-wave spectra of MTJ nanopillars as eigenexcitations of a coupled three-layer system with lateral confinement. In this section, we will see, which properties of the experimental spectra can be explained in the scope of this analytical model and which cannot. First, we will discuss the material parameters of the pillar extracted from the high-field regions of the spin-wave spectra. Thereafter, the low-field anomaly of the spectra and its relevance for applications will be discussed. Finally, we will summarize the properties of the experimental spectra, which are beyond the approximations of our model, including the pillar size dependence.

A. Material and geometry parameters

In this section, we will discuss the physical relevance of the extracted parameter values of the pillar in Table II. With 1.27 T, the saturation magnetization of the $Co_{60}Fe_{20}B_{20}$ layers of the pillar is significantly reduced compared to the thin-film value of (1.8 ± 0.1) T (Refs. 19 and 28) or the bulk value for the underlying $Co_{75}Fe_{25}$ of (2.2 ± 0.1) T.[29,30] A reduction in the magnetization in nanopillars has already been observed in previous studies on pillar devices.[14,16,31] Three scenarios are usually suggested to account for this phenomenon: process-induced damages,[19,32] current-induced heating,[33,34] or a nonlinear change in the frequency with high mode amplitude.[35] As we work with low bias current, current-induced heating can be excluded in our case. Similarly, since spin-torque-induced auto-oscillations in our samples occur typically for currents above 1.6 mA for size L,[23] high amplitude nonlinear effects as possible cause can be rejected, too. Therefore, some sort of process damage, such as ion implantation, diffusion, intrinsic chemical modifications, or interface effects, must be at the origin of the magnetization reduction, whose further investigation exceeds the scope of this paper.

Concerning the boundary conditions and exchange stiffness, we have come to the following conclusions: Strong pinning can be ruled out in our pillars (see Sec. VI); reasonable agreement between calculated and experimental data is obtained under the assumption of weak pinning. The pinning parameter deduced from the extracted mode numbers is with $d \leq 1$ about ten times smaller than the one calculated by means of Eq. (5) in Ref. 9 ($d \approx 10$) when using the material parameters of Table II. Any value of d substantially larger than 3 is found to yield mode numbers for the lowest mode very close to 1, i.e., strong pinning. This discrepancy between our result and the predictions of Guslienko's analytical model[9] is not understood, as the latter is expected to be valid in the regime of element thicknesses smaller than the exchange length as well.

We emphasize that, just as the magnetization, the exchange stiffness of the free layer does not exceed 2/3 of the thin-film value, independent of the boundary conditions. Therefore, the magnetic properties of the nanopillar can by no means be described by the values measured on the unpatterned thin films.

The mutual dipolar coupling accounts for several features of the experimental spectra. In the HA spectra, the mutual dipolar coupling of the FL and the SAF raises the frequency minima of F0 by several gigahertz, pushes them to slightly higher fields, and lowers the slope of the modes, reducing their frequency at ± 190 mT by about 1 GHz. It also causes the bell shape of the HA hysteresis loop, by forcing the pillar into the AP state at low fields, and smoothes out the sharp bends at the anisotropy fields, which are observed in the case of an uncoupled free layer.

In the EA spectra, the gap openings in the mode F0 stem from the anticrossing of F0 with the acoustic SAF modes due to coupling-induced mode hybridization. Finally, the net dipolar coupling field created by the SAF layers and favoring the antiparallel configuration of the pillar causes a shift of 5 mT of the EA hysteresis loops to negative fields, which is approximately 50% of the observed total shift. The remaining 50% may be due to an unequal reduction in the coercive fields at positive and negative fields, which occurs if the micromagnetic configuration causes the FL to switch more easily from the P state to the AP state, than from the AP state to the P state. Indeed, the FL magnetization is expected to be more nonuniform—and consequently easier to switch—in the low-field P state because of the mutual dipolar coupling field pointing antiparallel to the magnetizations in the P state but parallel in the AP state.

Within the diagonal tensor approximation of the mutual dipolar coupling, the tensor components are found to be significantly smaller than the values predicted by the formalism developed by Newell *et al.*[25] or by the simplified version using for the in-plane components of the mutual dipolar coupling tensor the corresponding components of the self-demagnetizing tensor, as is commonly practiced when modeling flip-flop switching in magnetoresistive random access memory cells.[36,37] The coupling between, e.g., the free layer and the reference layer of our pillars would be overestimated by Ref. 25 by a factor of 2, and by Refs. 36 and 38 by a factor of 3. A possible explanation for this reduction in the interlayer dipolar coupling may be that the coupling field extracted from the experiment is actually an *effective* mutual dipolar coupling field comprising the dipolar coupling due to the charges at the lateral layer boundaries as well as some Néel-type coupling resulting from the correlated roughness of the three magnetic layers. This orange-peel coupling may partially compensate the antiparallel coupling due to the charges at the layer edges. Another possibility is a reduction in the dipolar coupling due to the nonuniformity of the micromagnetic magnetization at the layer edges, though this effect should be small at high fields.

Finally, the extracted exchange-bias energy and the interlayer exchange coupling are consistent with the large body of dedicated literature (see, e.g., the values in Appendix B 2).

B. Low-field behavior and its relevance for applications

In Secs. II and III, we have seen that at low fields, both EA and HA spectra show for all three pillar sizes unmistakable signs of nonuniform magnetizations: in the HA spectra, the FL modes possess at zero field, instead of the local maximum predicted by the model, sharp minima, whose depth increases with increasing pillar size, indicating increasing nonuniformity of the magnetization. In fact, the modes F0 and F1 are likely to change character from volume modes at high and medium fields to edge modes at low field. The EA spectra contain low-frequency edge modes FE, which become progressively deformed around zero field for increasing pillar size, i.e., for increasing nonuniformity of the magnetization.

The nonuniformities of the magnetizations are expected to influence the switching dynamics of the pillar. The first consequence is that they lower the coercive field (as discussed in the previous paragraph), thus enlarging its difference to the shape anisotropy field. This effect has indeed been found to be particularly strong for size L (see Sec. II). More importantly, the fact that the lowest mode is not the uniform mode

but an edge mode, will affect the magnetization reversal path in current-induced switching, favoring nonuniform reversal paths, as has already been concluded indirectly from reversal speed experiments.[39]

C. Spin-wave phenomena beyond the analytical approximations

Based on the assumption of macrospin equilibrium magnetizations, our model is certain not to describe any effect resulting from nonuniformities of the magnetization. This is the case, e.g., for the low-field behavior discussed in the previous paragraph, or the occurrence of more than one spin-flop transition of the SAF at positive EA field. However, even for high fields and pillar size S where the model is expected to work reasonably well, there are qualitative discrepancies between calculated and experimental spectra in frequency or visibility of higher-order modes.

Similarly, the high-field evolution of the spin-wave spectra with the pillar size is not consistent with the predictions by the model. Although the model allows to reproduce qualitatively the EA spectra for pillar size L under reasonable assumptions, it fails for the high-field HA spectra.

VIII. CONCLUSIONS

In this paper, we have studied the magnetic field dependence of the mode frequency of thermally excited spin waves in rectangular-shaped MgO-MTJ nanopillars of different lateral sizes. The spin-wave spectra (frequency versus easy-axis and hard-axis applied field) of individual devices were obtained using spectrally resolved electrical-noise power measurements.

In all spectra, several independent quantized spin-wave modes stemming from eigenexcitations in the free layer and the SAF layers of the MTJ have been observed. By diagonalizing the dynamical matrix of a system of three coupled, spatially confined magnetic layers, we have modeled the mode frequencies for the smallest pillar size, $60 \times 100 \text{ nm}^2$, obtaining quantitative agreement for a majority of modes at high and medium applied fields. Our ability to detect a particular spin-wave mode depends on the static micromagnetic configuration of the layers as well as on the symmetry properties of the mode. With the help of these discrimination criteria, we could identify the observed modes and extract the material parameters of the pillar (Table II). The magnetizations and exchange stiffness constants were found to be significantly reduced compared to the corresponding thin-film values whereas the interlayer exchange coupling and the exchange bias are consistent with their thin-film counterparts. The interlayer dipolar coupling between the different layers could be well described in terms of an effective mutual dipolar coupling. Moreover, we could infer that the pinning of the magnetizations at the lateral boundaries must be weak.

Finally, at low fields and for larger pillar sizes, there is clear evidence for strong nonuniformities of the layer magnetizations, leading to qualitative differences between calculated and measured spin-wave frequencies.

APPENDIX A: DERIVATION OF MAGNETORESISTANCE NOISE SIGNATURE

In this appendix we derive Eq. (7) and the leading-order terms in Table I starting from Eq. (6) The first step is to evaluate the dot product in Eq. (6) of the dynamical magnetization $\delta \vec{M}_F^U(\vec{k})$ of the FL with the equilibrium magnetization $\vec{M}_1(\vec{r})$ of the RL. Since $\delta \vec{M}_F^U(\vec{k})$ is perpendicular to the macrospin component $\vec{M}_F^U$, the dot product of $\delta \vec{M}_F^U(\vec{k})$ with $\vec{M}_1^U$ can be expressed in terms of the angle θ between the macrospins $\vec{M}_F^U$ and $\vec{M}_1^U$ of the two layers. Similarly, decomposing $\delta \vec{M}_1^E(\vec{r})$ into a component $\delta M_{1,\parallel}^E(\vec{r})$ parallel to the macrospin $\vec{M}_1^U$, and a component $\delta M_{1,\perp}^E(\vec{r})$ perpendicular to $\vec{M}_1^U$, allows to evaluate the dot product of $\delta \vec{M}_1^E(\vec{r})$ with $\delta \vec{M}_F^U(\vec{k})$. With that the MR variation (6) becomes

$$\delta R_F(\vec{k}, \theta) = \delta M_F^U(\vec{k})[\overline{M_1^V}(\vec{k}, \theta) + \overline{M_1^E}(\vec{k}, \theta)], \quad (A1)$$

where

$$\overline{M_1^V}(\vec{k}, \theta) = \sin \theta M_1 \bar{W}_x(n_x, \phi_x) \bar{W}_y(n_y, \phi_y), \quad (A2)$$

$$\bar{W}_x(n_x, \phi_x) \bar{W}_y(n_y, \phi_y) = \frac{1}{S_{pil}} \int_{S_{pil}} \Re e^{i\vec{k}\vec{r}} d\vec{r}, \quad (A3)$$

and

$$\overline{M_1^E}(\vec{k}, \theta) = \frac{1}{S_{pil}} \int_{S_{pil}} [\cos \theta \delta M_{1,\perp}^E(\vec{r}) + \sin \theta \delta M_{1,\parallel}^E(\vec{r})] \Re e^{i\vec{k}\vec{r}} d\vec{r}.$$

$$(A4)$$

As the edge-domain contributions [Eq. (A4)] are relevant only on the EA in P and AP states where θ is basically 0 or π, the term with $\sin \theta$ in Eq. (A4) is in all practical cases negligible, such that only the term $\delta M_{1,\perp}^E(\vec{r}) = \delta M_{1,y}^E(x, y)$ remains.

In the following, we derive the leading-order terms of these quantities listed in Table I.

1. Micromagnetic configuration dependence

Decomposing θ into the angle θ_0 between the two macrospins for an ideal pillar, and a small deviation $\Delta \theta$ due to misalignments, $\sin \theta$ and $\cos \theta$ in $\overline{M_1^V}(\vec{k}, \theta)$ and $\overline{M_1^E}(\vec{k}, \theta)$ can be expanded in $\Delta \theta$ about θ_0, where the leading-order terms for the different field regions are summarized in Table I. The underlying values of θ_0 are as follows: for EA applied field, $\theta_0 = 0$ in the P state, $\theta_0 = \pi$ in the AP state, and $0 \leqslant \theta_0 < \pi$

above the SF at positive fields, and below the secnd SF at negative fields. For HA field, θ_0 decreases continuously from π at zero field to a value close to $\pi/2$ at the saturation field of the FL, and finally toward zero as the RL magnetization continues to tilt toward the HA.

The presence of edge domains on the EA can be deduced from the hysteresis loops: deviations of the resistance from its saturation values in P and AP states indicate nonuniformities of the FL and/or the RL magnetization. For example, in the P state, the resistance increases continuously when the (ascending) field approaches the switching field to the AP state, both magnetizations being subject to an increasing effective antiparallel field consisting of the (self-)demagnetizing field, the mutual dipolar coupling field, and the external field as soon as it becomes positive.

In the AP state, at low negative field just before the switching to the P state, both the external field and the interlayer dipolar coupling field are parallel to the magnetization of the RL, thus partly suppressing the edge domains created by the (self-)demagnetizing field; in contrast, edge domains in the FL are only suppressed by the interlayer dipolar coupling field but enhanced by the external field. Indeed, the resistance in the low-field AP sate departs much less from AP remanence than it does from the P remanence in the low-field P state.

Finally, in the high-field AP state, the resistance starts to decrease continuously already long before the SF transition due to increasing nonuniformities of the RL magnetization, which is pointing antiparallel to the high external field.

On the HA, edge-domain contributions are negligible compared to the zeroth-order contributions of the volume magnetization, except for zero field where the macrospins are antiparallel.

2. Mode character dependence

By means of Eqs. (3) and (5), the two integrals $\bar{W}_x$ and $\bar{W}_y$ over the layer dimension in directions x and y, respectively, are easily evaluated as

$$\bar{W}_x(n_x, \phi_x) = \frac{2}{n_x \pi} \sin\left(n_x \frac{\pi}{2}\right) \sin \phi_x, \qquad \text{(A5)}$$

where $\bar{W}_y(n_y, \phi_y)$ is given by an analogous expression.

Decomposing the mode numbers and the phase as in Sec. V A, $n_x = n_x^0 + \Delta n_x$ and $\phi_x = \phi_x^0 + \Delta\phi_x$, where $\phi_x^0 = \pi/2 + n_x^0 \cdot \pi/2$ is the phase for symmetric pinning, $\bar{W}_x(n_x, \phi_x)$ can be expanded in $\Delta\phi_x \ll 1$ and either $\Delta n_x \ll 1$ (weak pinning) or $(1 - \Delta n_x) \ll 1$ (strong pinning). The result as a function of n_x is shown in Table I(b).

The edge-domain contributions $\overline{\delta M_l^E}$ to the MR noise in the P and AP states can be evaluated on the basis of symmetry considerations. In spite of a nonuniform equilibrium magnetization, $\overline{\delta M_l^E}$ is zero if the product of the wave function and the function describing the spatial dependence of the y component of the edge-domain magnetization under the integral [Eq. (A4)] is either zero or antisymmetric in x or y coordinate. For strong pinning, the product of the two functions is zero (or negligibly small) because near the layer

edges, where the edge-domain magnetization is nonzero, the wave function has minimum amplitude due to the pinning. Significant contributions from edge domains can be expected for weak pinning only. In this case, the integral [Eq. (A4)] will vanish for certain modes if the magnetization for a given micromagnetic state is invariant under reflection or rotation or a combination of both. The flower state, e.g., is invariant under reflections about x and y axes, i.e., the y component of the magnetization is antisymmetric in both x and y coordinates. $\overline{\delta M_l^E}$ is therefore nonzero only for modes with two odd mode numbers. Similarly, it can be shown that for the S state, $\overline{\delta M_l^E}$ is nonzero for modes, whose mode numbers are either both odd or both even; the C state renders modes with odd n_x visible.

Finally, we derive the expected relative intensity of the modes. Δn_x for weak pinning or $(1 - \Delta n_x)$ for strong pinning are of the order 0.1. We may assume that for small asymmetries of the pinning, $\Delta\phi_x$ is at most of the same order of magnitude as Δn_x (or $(1 - \Delta n_x)$). Therefore, for weak pinning, $\bar{W}_x(n_x^0 \geq 1) \approx 0.1/n_x$ is one order of magnitude smaller than $\bar{W}_x(n_x^0 = 0) \approx 1$, and we expect to observe in addition to the quasiuniform mode close to (0,0) higher modes with mode numbers close to (1,0), (0,1), (2,0), (0,2), and possibly (3,0). Their intensities, being proportional to $(\bar{W}_x \bar{W}_y)^2$, scale with factors quadratical in $\Delta\phi_{x,y}$ or $\Delta n_{x,y}$, and are therefore two orders of magnitude lower than that of (0,0). The intensities of all other modes, such as (1,1), are of forth order in $\Delta\phi_{x,y}$ and $\Delta n_{x,y}$, or strongly reduced by the factor $1/(n_x n_y)^2$, and therefore most likely too weak to be detected.

For strong pinning and even n_x^0, $\bar{W}_x(n_x^0 \geq 1) \approx 1/n_x$ is of the same order of magnitude as $\bar{W}_x(n_x^0 = 0) \approx 1$. In contrast, for odd n_x^0, $\bar{W}_x(n_x^0 \geq 1) \approx 0.01/n_x$ is two orders of magnitude smaller than $\bar{W}_x(n_x^0 = 0)$. Consequently, the higher modes close to (3,1), (1,3), and (5,1) will have intensities comparable to that of the fundamental mode close to (1,1), or one order of magnitude lower due to the factor $1/(n_x n_y)^2$.

APPENDIX B: DETAILS ON EXTRACTION OF MODEL PARAMETERS

In this annex, we present the arguments used to extract the material parameters M_l, A_l, J^{eb}, and J^{int}, the geometry parameters (N_l^x, N_l^y, N_l^z) and $(N_{ml}^x, N_{ml}^y, N_{ml}^z)$, as well as the mode numbers (n_x, n_y) from the experimental spectra.

1. Reduction in number of free parameters

Given the (approximate) layer dimensions L_x, L_y, L_z, the demagnetizing factors N_l^x, N_l^y, and N_l^z can be calculated using, e.g., OOMMF simulations, where we find $N_l^z \approx 1 - (N_l^x + N_l^y)$ and $N_l^y/N_l^x \approx L_x/L_y$ as should be expected. Using the formulas in Ref. 25 it can be shown that the dipolar coupling constants obey similar relations, $N_{ml}^y/N_{ml}^x = L_x/L_y$ and $N_{ml}^z = -(N_{ml}^x + N_{ml}^y)$, and for symmetry reasons, $\mathbf{N}_{ml} = \mathbf{N}_{lm}$. The remaining components N_{F1}^x, N_{F2}^x, and N_{12}^x are kept as free parameters to be extracted from the experiment, although they can be calculated by means of Ref. 25.

On the basis of previous measurements on MTJ stacks, the number of free parameters can be further reduced: In Ref. 26, it has been shown that the magnetization of the CoFeB free layer does not depend on the layer thickness in the range from 2 to 3 nm. We may therefore assume that the FL and the RL—being of the same material but having different thicknesses—have equal magnetizations, $M_1 = M_F$. Moreover, we expect the layer magnetizations in the pillar to be reduced for all layers by the same (relative) amount w.r.t. the thin-film saturation magnetizations, $M_2^{pillar}/M_2^{film} = M_{F,1}^{pillar}/M_{F,1}^{film}$. Analogous relations are expected to hold for the exchange stiffness constants A_l: $A_1 = A_F$ and $A_2^{pillar}/A_2^{film} = A_{F,1}^{pillar}/A_{F,1}^{film}$.

2. Literature values

In this paragraph, we list as an orientation literature values for the material parameters. As thin-film exchange stiffness constants we use the values of the 40 nm CoFeB and CoFe films in Ref. 28: $A_{F,1}^{film} = 28.4 \times 10^{-12}$ J/m and $A_2^{film} = 27.5 \times 10^{-12}$ J/m.

The magnetizations of CoFe and annealed CoFeB depend on the percentage of Fe in Co. The bulk value for both $Co_{70}Fe_{30}$ and $Co_{75}Fe_{25}$ (corresponding to $Co_{60}Fe_{20}B_{20}$) is (2.2 ± 0.1) T.[29,30] The (thin-film) free layer magnetization of our MTJ stack has been measured to be $\mu_0 M_F^{film} = (1.8 \pm 0.1)$ T.[19] The thin-film value for the CoFe layer is expected to be in the interval $\mu_0 M_2^{film} = (2.0 \pm 0.2)$ T.

The exchange-bias field in a $Co_{90}Fe_{10}$ (5 nm)/PtMn (20 nm) system has been measured to be $\mu_0 H^{eb} \approx 67$ mT,[40,41] which corresponds to an exchange-bias energy of $J^{eb} = 4.5 \times 10^{-4}$ J/m^2, using 2.0 T as saturation magnetization of the CoFe layer. For the interlayer exchange energy, a maximum value of $J^{int} = -5 \times 10^{-4}$ J/m^2 has been reported.[42]

Reference 25 allows to calculate the dipolar coupling constant for two rectangular layers of equal thicknesses. As in our pillars the FL has a different thickness than the two SAF layers, only N_{12}^x may be calculated directly, yielding $N_{12}^x = 0.016$. The dipolar coupling constants N_{F1}^x and N_{F2}^x involving the FL can only be estimated as the mean value of the constants calculated for two 3-nm-thick layers and for two 2-nm-thick layers, from which we obtain $N_{F1}^x \approx 0.018$ and $N_{F2}^x \approx 0.013$ (maximum deviation ± 0.003).

3. Regression method

M_F is determined by the modes F0 on the EA with a weak dependence on the chosen mode numbers of F0 (see discussion below). A minimum value for M_F of 1.25 T follows from the measured room-temperature anisotropy field, which must be smaller than the calculated (zero-temperature) anisotropy field. M_1 and M_2 cannot be extracted directly but depend entirely on the above assumptions. Once M_1 and M_2 have been fixed, J^{int} and J^{eb} can be estimated from the spin-flop field and the mode A0 on the HA. N_{F1}^x and N_{F2}^x follow from the gap opening in the mode F0 on the EA and the shift of the EA hysteresis loop to negative fields: We have used the above calcuted values for N_{F1}^x, N_{F2}^x, and N_{12}^x as starting values, which we have adapted to the experimental data by rescaling, assuming that the deviation of the mutual dipolar fields, e.g., due to micromagnetics, is similar for all pillar layers. It turns out that N_{F1}^x as the largest component can be maximum 0.01 because otherwise the gap opening exceeds the observed 2 GHz (maximum value of 2.5 GHz for the calculated coefficients). On the other hand, the difference of N_{F1}^x and N_{F2}^x must be at least 0.005 to ensure a shift of the hysteresis loop of minimum 5 mT. $N_{F1}^x = 0.01$ and $N_{F2}^x = 0.005$ are therefore uniquely determined (maximum deviation ± 0.002). Since for the calculated constants N_{12}^x is between N_{F1}^x and N_{F2}^x, we set $N_{12}^x = 0.007$.

The exchange stiffness constant A_F and the mode numbers (n_x, n_y) cannot be extracted separately since they enter the effective field (and consequently the frequencies) only as a product. The BC in the pillar being unknown, the lowest modes can have any mode numbers between (0,0) (unpinned BC) and (1,1) (totally pinned BC), where n_x can be larger than n_y (cf. Sec. V A).

In order to adjust F0 on the EA with the mode (1,1) in the limit of strong pinning, we would need $A_F \approx (1/20)A_F^{film}$ and $\mu_0 M_F \approx 1.1$ T; this value for M_F is significantly smaller than the allowed minimum, and the reduction in A_F w.r.t. its thin-film value is unreasonably large given that $M_F \approx (2/3)M_F^{film}$. In addition, a discrepancy of more than 1.5 GHz between calculated and measured mode F0 is observed on the HA even at high fields. Similarly, fitting F0 with the mode (0.5,0.5), which might be considered as the border between strong and weak pinning for $n_x = n_y$, or the mode (1,0), for maximum difference $n_x - n_y$, still requires $A_F < (1/5)A_F^{film}$ and $\mu_0 M_F \approx 1.2$ T. Consequently, strong pinning can be excluded in our pillars; the mode numbers of F0 must be well below (0.4,0.4) or (0.8,0). The pinning is weak. This is also corroborated by the fact that, in particular, on the HA the lowest mode F0 has much higher intensity than the higher modes F1 to F5, which is a characteristics of weakly pinned systems (cf. Sec. V B).

If we assume totally unpinned BC—fitting F0 with (0,0) and the higher modes with (1,0), (0,1). etc.—we get $\mu_0 M_F = 1.3$ T and $A_F \approx (2/3)A_F^{film}$, i.e., approximately $A_F \propto M_F$. To narrow the mode numbers down within these borders, we assume that indeed $n_x > n_y$, which finally confines (n_x, n_y) on the HA to $(n_x, n_y) \leq (0.2, 0.1)$ and on the EA to $(n_x, n_y) \leq (0.4, 0.2)$. To fit F0 on EA and HA simultaneously, requires that the mode numbers on the HA are smaller than on the EA, as had already been suggested in Sec. V A.

*annerose.helmer@u-psud.fr

[1] J. Katine and E. E. Fullerton, J. Magn. Magn. Mater. **320**, 1217 (2008).

[2] C. Chappert, A. Fert, and F. N. Van Dau, Nature Mater. **6**, 813 (2007).

[3] A. M. Deac, A. Fukushima, H. Kubota, H. Maehara, Y. Suzuki, S. Yuasa, Y. Nagamine, K. Tsunekawa, D. D. Djayaprawira, and N. Watanabe, Nat. Phys. **4**, 803 (2008).

[4] C. Bayer, J. Jorzick, S. O. Demokritov, A. N. Slavin, K. Y. Guslienko, D. V. Berkov, N. L. Gorn, M. P. Kostylev, and B. Hillebrands, in *Spin Dynamics in Confined Magnetic Structures III*, Topics in Applied Physics Vol. 101 (Springer-Verlag, Berlin Heidelberg, 2006), pp. 57–103.

[5] M. Bailleul, R. Höllinger, and C. Fermon, Phys. Rev. B **73**, 104424 (2006).

[6] G. Gubbiotti, M. Madami, S. Tacchi, G. Carlotti, A. Adeyeye, S. Goolaup, N. Singh, and A. Slavin, J. Magn. Magn. Mater. **316**, e338 (2007).

[7] G. Gubbiotti, G. Carlotti, T. Okuno, M. Grimsditch, L. Giovannini, F. Montoncello, and F. Nizzoli, Phys. Rev. B **72**, 184419 (2005).

[8] F. Montoncello, L. Giovannini, F. Nizzoli, P. Vavassori, M. Grimsditch, T. Ono, G. Gubbiotti, S. Tacchi, and G. Carlotti, Phys. Rev. B **76**, 024426 (2007).

[9] K. Y. Guslienko and A. N. Slavin, Phys. Rev. B **72**, 014463 (2005).

[10] P. Vavassori, V. Bonanni, A. Busato, D. Bisero, G. Gubbiotti, A. O. Adeyeye, S. Goolaup, N. Singh, C. Spezzani, and M. Sacchi, J. Phys. D **41**, 134014 (2008).

[11] G. Gubbiotti, M. Madami, S. Tacchi, G. Carlotti, and T. Okuno, Phys. Rev. B **73**, 144430 (2006).

[12] G. Gubbiotti, M. Madami, S. Tacchi, G. Socino, G. Carlotti, and T. Ono, J. Appl. Phys. **101**, 09F502 (2007).

[13] P. Vavassori, V. Bonanni, A. Busato, G. Gubbiotti, M. Madami, A. O. Adeyeye, S. Goolaup, N. Singh, C. Spezzani, and M. Sacchi, J. Appl. Phys. **103**, 07C512 (2008).

[14] S. Petit, C. Baraduc, C. Thirion, U. Ebels, Y. Liu, M. Li, P. Wang, and B. Dieny, Phys. Rev. Lett. **98**, 077203 (2007).

[15] A. V. Nazarov, H. S. Cho, J. Nowak, S. Stokes, and N. Tabat, Appl. Phys. Lett. **81**, 4559 (2002).

[16] Y. Guan, J. Z. Sun, X. Jiang, R. Moriya, L. Gao, and S. S. P. Parkin, Appl. Phys. Lett. **95**, 082506 (2009).

[17] J. C. Sankey, P. M. Braganca, A. G. F. Garcia, I. N. Krivorotov, R. A. Buhrman, and D. C. Ralph, Phys. Rev. Lett. **96**, 227601 (2006).

[18] S. Petit, N. de Mestier, C. Baraduc, C. Thirion, Y. Liu, M. Li, P. Wang, and B. Dieny, Phys. Rev. B **78**, 184420 (2008).

[19] S. Cornelissen, L. Bianchini, A. Helmer, T. Devolder, J.-V. Kim, M. O. de Beeck, W. V. Roy, L. Lagae, and C. Chappert, J. Appl. Phys. **105**, 07B903 (2009).

[20] T. Devolder *et al.*, J. Appl. Phys. **103**, 07A723 (2008).

[21] T. Devolder, P. Crozat, C. Chappert, J. Miltat, A. Tulapurkar, Y. Suzuki, and K. Yagami, Phys. Rev. B **71**, 184401 (2005).

[22] N. Smith, J. Appl. Phys. **90**, 5768 (2001).

[23] S. Cornelissen, L. Bianchini, G. Hrkac, M. O. de Beeck, L. Lagae, J.-V. Kim, T. Devolder, P. Crozat, C. Chappert, and T. Schrefl, EPL **87**, 57001 (2009).

[24] G. Counil, J.-V. Kim, T. Devolder, P. Crozat, C. Chappert, and A. Cebollada, J. Appl. Phys. **98**, 023901 (2005).

[25] A. J. Newell, W. Williams, and D. J. Dunlop, J. Geophys. Res. **98**, 9551 (1993).

[26] H. Kubota, A. Fukushima, Y. Ootani, S. Yuasa, K. Ando, H. Maehara, K. Tsunekawa, D. D. Djayaprawira, N. Watanabe, and Y. Suzuki, Appl. Phys. Lett. **89**, 032505 (2006).

[27] M. P. Kostylev, G. Gubbiotti, J.-G. Hu, G. Carlotti, T. Ono, and R. L. Stamps, Phys. Rev. B **76**, 054422 (2007).

[28] C. Bilzer, T. Devolder, J.-V. Kim, G. Counil, C. Chappert, S. Cardoso, and P. P. Freitas, J. Appl. Phys. **100**, 053903 (2006).

[29] R. M. Bozorth, *Ferromagnetism* (IEEE, New York, 1993).

[30] Y. Lamy and B. Viala, J. Appl. Phys. **97**, 10F910 (2005).

[31] S. I. Kiselev, J. C. Sankey, I. N. Krivorotov, N. C. Emley, M. Rinkoski, C. Perez, R. A. Buhrman, and D. C. Ralph, Phys. Rev. Lett. **93**, 036601 (2004).

[32] I. N. Krivorotov, N. C. Emley, J. C. Sankey, S. I. Kiselev, D. C. Ralph, and R. A. Buhrman, Science **307**, 228 (2005).

[33] D. H. Lee and S. H. Lim, Appl. Phys. Lett. **92**, 233502 (2008).

[34] T. Devolder, J.-V. Kim, C. Chappert, J. Hayakawa, K. Ito, H. Takahashi, S. Ikeda, and H. Ohno, J. Appl. Phys. **105**, 113924 (2009).

[35] Q. Mistral, J.-V. Kim, T. Devolder, P. Crozat, C. Chappert, J. A. Katine, M. J. Carey, and K. Ito, Appl. Phys. Lett. **88**, 192507 (2006).

[36] D. C. Worledge, Appl. Phys. Lett. **84**, 4559 (2004).

[37] D. C. Worledge, P. L. Trouilloud, and W. J. Gallagher, Appl. Phys. Lett. **90**, 222506 (2007).

[38] D. C. Worledge, Appl. Phys. Lett. **84**, 2847 (2004).

[39] T. Devolder, J. Hayakawa, K. Ito, H. Takahashi, S. Ikeda, P. Crozat, N. Zerounian, J.-V. Kim, C. Chappert, and H. Ohno, Phys. Rev. Lett. **100**, 057206 (2008).

[40] M. Rickart, A. Guedes, B. Negulescu, J. Ventura, J. Sousa, P. Diaz, M. MacKenzie, J. Chapman, and P. Freitas, Eur. Phys. J. B **45**, 207 (2005).

[41] J. M. Teixeira *et al.*, Eur. Phys. J. B **82**, 1486 (2008).

[42] S. S. P. Parkin, N. More, and K. P. Roche, Phys. Rev. Lett. **64**, 2304 (1990).